

Electronic Supplementary Information

Controlling the speciation and reactivity of carbon-supported gold nanostructures for catalysed acetylene hydrochlorination

*Selina K. Kaiser,^{‡a} Ronghe Lin,^{‡a} Sharon Mitchell,^a Edvin Fako,^b Frank Krumeich,^a Roland Hauert,^c Olga V. Safonova,^d Vita A. Kondratenko,^e Evgenii V. Kondratenko,^e Sean M. Collins,^f Paul A. Midgley,^f Núria López^b and Javier Pérez-Ramírez^{*a}*

^aInstitute for Chemical and Bioengineering, Department of Chemistry and Applied Biosciences, ETH Zurich, Vladimir-Prelog-Weg 1, 8093 Zurich, Switzerland

^bInstitute of Chemical Research of Catalonia (ICIQ), The Barcelona Institute of Science and Technology, Av. Països Catalans 16, 43007 Tarragona, Spain

^cSwiss Federal Laboratories for Materials Science and Technology, EMPA, Überlandstrasse 129, 8600 Dübendorf, Switzerland

^dPaul Scherrer Institut, 5232 Villigen PSI, Switzerland

^eLeibniz-Institut für Katalyse e. V., Albert-Einstein-Straße 29a, 18059 Rostock, Germany

^fDepartment of Materials Science and Metallurgy, University of Cambridge, 27 Charles Babbage Road, Cambridge CB3 0FS, United Kingdom

[‡]Equal contribution

*Corresponding author. E-mail: jpr@chem.ethz.ch

Experimental section

Catalyst synthesis

The N-doped carbon support (NC) was prepared in a two-step synthesis, comprising the oxidative polymerisation of aniline and a subsequent carbonisation step.¹ Aniline (50 mmol, Acros, 99.5%) was dissolved in deionised water (40 cm³, pH 0.4; adjusted by hydrochloric acid, 1.25 M, Sigma Aldrich, >37%), cooled to 277 K, and subsequently added to a precooled solution (277 K) of ammonium persulfate (100 mmol, Acros, 98%) in deionised water (20 cm³). After 1 h of vigorous stirring, the mixture was kept at room temperature for 24 h to complete the polymerisation process. The formed polyaniline was thoroughly washed with deionised water for neutralisation, dried in static air at 393 K for 12 h, and afterwards calcined at 1073 K (heating rate 5 K min⁻¹, 1 h, N₂ atmosphere). The obtained N-doped carbon was ground and sieved (400-600 microns) to ensure a uniform particle size fraction. In order to minimise changes in the porous properties during thermal activation, the NC support was immersed in aqua regia, dried in air at room temperature, and subsequently calcined at 673 K (heating rate 5 K min⁻¹, 16 h, N₂ atmosphere). The commercial activated carbon support (Norit ROX 0.8) was immersed in aqua regia at room temperature to remove metal impurities such as Na, Fe, and Cu. After filtration and thorough washing with deionised water (2 L g⁻¹), the material was dried in static air at 393 K for 12 h. NC-I was synthesised following a similar protocol to NC, except that the calcination was conducted at a higher temperature of 1273 K, resulting in a decreased N-content. NC-II and NC-III were prepared *via* the post-synthetic activation of the NC and NCI supports, respectively, at 1073 K (heating rate 10 K min⁻¹, 1 h, N₂ atmosphere) in order to increase the surface area and pore volume of these samples.

All gold catalysts were prepared following the incipient wetness impregnation method reported by Hutchings and coworkers (nominal gold loading of 0.5 wt.%).²⁻³ Accordingly, a solution of the gold precursor, HAuCl₄·xH₂O (ABCR, 99.9%, 49.5 wt.% Au), dissolved in aqua regia (1.5 mL g⁻¹), was added dropwise to the AC or NC carriers under continuous stirring for 30 min. Subsequently, all samples were thermally activated at distinct temperatures, as indicated in the respective sample code (Au/NC-*T* or Au/AC-*T* where *T* = 413-1073 K, 16 h, static air when *T* ≤ 473 K and N₂ atmosphere when *T* > 473 K). For all other catalysts Au/NC-I-III, as well as Au/NC-EtOH and Au/AC-EtOH a thermal

activation temperature of 473 K was selected. The latter were prepared by replacing aqua regia with ethanol in the above described impregnation step (Fisher, >99.8%).

Catalyst characterisation

Powder X-ray diffraction (XRD) was measured using a PANalytical X'Pert PRO-MPD diffractometer with Cu-K α radiation ($\lambda = 1.54060 \text{ \AA}$). The data was recorded in the $10\text{-}70^\circ$ 2θ range with an angular step size of 0.017° and a counting time of 0.26 s per step. Argon sorption was measured at 77 K in a Micrometrics 3Flex instrument, after evacuation of the samples at 423 K for 12 h. Elemental analysis (C, H, N) was determined by infrared spectroscopy using a LECO TruSpec Micro combustion furnace. Scanning transmission electron (STEM) micrographs with a high-angle annular dark-field (HAADF) detector were acquired on a HD2700CS (Hitachi) microscope operated at 200 kV. Samples were prepared by dipping the copper grid in a suspension of the solid in ethanol and drying in air. Aberration-corrected (AC-STEM) was performed using an FEI Titan 80-300 electron microscope equipped with a high-brightness X-FEG electron source and a CEOS aberration corrector for the probe-forming lenses. The microscope was operated at 300 kV with an illumination semi-angle of 17.5 mrad , a probe current of $\approx 60 \text{ pA}$, and a pixel dwell time of $8 \text{ }\mu\text{s}$. To gain further insight into the stability of gold single atoms hosted on N-doped carbon, time-series multi-frame AC-STEM imaging (AC-STEM video imaging) was acquired for Au/NC-413 and Au/NC-1073. A 300 kV electron beam imparts up to 4 eV to metal atoms in the sample,⁴ and therefore induces metal atom motion. This electron beam-induced atomic motion observed in STEM can be used to reveal characteristics of atomic surface diffusion and coordination sites.⁵ AC-STEM videos were acquired using identical electron optical conditions as for single-frame imaging, but with a pixel dwell time of $3 \text{ }\mu\text{s}$. Each sample region used for AC-STEM video imaging was scanned over an area with dimensions 512×512 pixels with a pixel size of 0.018 nm for 40 consecutive frames. Three such data-sets each were analysed from different regions of Au/NC-413 and Au/NC-1073 samples (six regions in total). Image-series were first processed by cross-correlation with a two-dimensional Gaussian function tuned to the approximate size of the gold atoms (**Videos S1** and **S2**). Image-series were then processed using TrackPy, an open-source particle tracking toolkit implemented in Python. For Au/NC-413, 297 atom trajectories were identified and analysed in terms

of the mean squared displacement (MSD). For Au/NC-1073, 272 atom trajectories were analysed. Drift between frames was corrected prior to determination of MSD by vectorial subtraction of the average displacement in each frame. Due to carbon contamination under electron beam irradiation, particularly for the Au/NC-413 sample, only the first 10 s of the video was used for power-law fitting according to the relationship $MSD = A t^n$, where A is a term related linearly to the diffusivity ($A = 4D$ for diffusivity D), t is the lag time in seconds, and n is an exponent expected to be one ($n = 1$) for random (Brownian) motion. X-ray photoelectron spectra (XPS) were acquired on a Physical Electronics Quantum 2000 instrument using monochromatic Al-K α radiation, generated from an electron beam operated at 15 kV, and equipped with a hemispherical capacitor electron-energy analyser. The samples were analysed at the electron take-off angle of 45° and the pass energy of 46.95 eV. The spectrometer was calibrated for the Au 4f_{7/2} signal at 84.0 ± 0.1 eV with a resolution step width of 0.2 eV. The Au 4f and N 1s spectra were fitted by mixed Gaussian-Lorentzian component profiles after Shirley background subtraction. The selected peak positions of the different nitrogen species are based on literature reported data and fixed with an error of ±0.2 eV. The detailed fitting parameters, reported in literature and used in this work, are given in **Tables S1** and **S2**. The elemental concentrations were quantified based on the measured photoelectron peak areas (C 1s, N 1s, O 1s, Cl 2p, and Au 4f), using PHI-MultiPak software and the built-in relative sensitivity factors, which are corrected for the system transmission function. X-ray absorption fine structure (XAFS) measurements at the Au L₃-edge (11.919 keV) were carried out at the SuperXAS beamline⁶ at the Swiss Light Source (Villigen, Switzerland). The incident photon beam provided by a 2.9 T superbend magnet was selected by a Si(111) channel-cut Quick-EXAFS monochromator.⁷ The rejection of higher harmonics and focusing were achieved with rhodium-coated collimating and torroidal mirrors, respectively, at 2.5 mrad. The beamline was calibrated using Au foil. The area of sample illuminated by the X-ray beam was 0.5 mm × 0.2 mm with a total intensity of about 7×10¹¹ ph s⁻¹. The AC- and NC-supported samples (600 mg) were finely ground, mixed homogeneously with three parts of cellulose, and pressed into 13 mm diameter pellets. Commercial Au₂O₃ (Alfa Aesar, 99.99%) and AuCl₃ (ABCR, 99%) were used as references. All spectra were recorded in transmission mode at room temperature. The extended X-ray absorption fine structure (EXAFS) spectra were acquired with a 1 Hz frequency (0.5 s per spectrum) and then averaged over 5-15 min. Sample damage

by X-rays could be inhibited by fast data acquisition. Only in the case of AuCl₃ X-ray damage was observed and therefore the EXAFS spectra of this sample were averaged over 10 s. The X-ray absorption near-edge structure (XANES) spectra were calibrated by measuring gold foil simultaneously with each sample. The XAFS spectra were analysed using the Demeter software package.⁸ The background signal before the edge was subtracted using a linear function (fitting range between –132 and –30 eV). The post edge signal was normalised to the step of one after fitting it in the region between 150 and 1670 eV after the edge. We fitted the k^3 weighted Fourier transformed signal and determined an amplitude reduction factor (S_0^2) of 0.78 from EXAFS fit of the Au foil. For the Au/AC-413 and Au/NC-413 samples all EXAFS spectra were fitted in the k range of 3-16 Å⁻¹ and R range of 1-3 Å; for Au/NC-973 and Au/NC-1073 the k range was 3-12 Å⁻¹ and R range 1-2 Å. To fit the Au–Cl and Au–N(O) scattering paths we used Au₂O₃ and AuCl₃ structures as the references.

Catalyst testing under steady-state conditions

Steady-state acetylene hydrochlorination was studied in a continuous-flow fixed-bed micro-reactor at atmospheric pressure. The set-up (**Fig. S1**) consisted of (1) two-way valves and (2) digital mass-flow controllers (Bronkhorst) to feed C₂H₂ (PanGas, purity 2.6), HCl (Air Liquide, purity 2.8, anhydrous), Ar (PanGas, purity 5.0, internal standard), and He (PanGas, purity 5.0, carrier gas for kinetic studies), (3) a gas mixing unit, pressure indicator (PI), (4) a quartz micro-reactor of 10 mm inner diameter equipped with a K-type thermocouple (TI) with the tip positioned in the centre of the (5) catalyst bed, (6) a homemade electrical oven, (7) downstream heat lining operated at 393 K to avoid condensation of reaction products, (8) a three-way sampling valve, (9) a gas chromatograph equipped with a GS-CarbonPLOT column coupled to a mass spectrometer (GC-MS, Agilent, GC 7890B, Agilent MSD 5977A) with a triple-axis detector and electron multiplier for on-line analysis, and (10) impinging bottles containing concentrated NaOH solution for neutralisation of the effluent stream.

In a typical test, the catalyst ($W_{\text{cat}} = 100$ mg, particle size $d_p = 0.4$ -0.6 mm) was loaded in the quartz reactor and pre-treated in He at 393 K for 30 min. Thereafter, a total gas flow (F_T) of 15 cm³ min⁻¹, containing 40 vol.% C₂H₂, 44 vol.% HCl, and 16 vol.% Ar, was fed into the reactor at bed temperatures (T_{bed}) of 473 K and a gas hourly space velocity based on acetylene (GHSV(C₂H₂)) of 1500 h⁻¹. For the

stability tests the catalyst loading was increased to $W_{\text{cat}} = 250$ mg, giving a GHSV(C_2H_2) of 610 h^{-1} . Reaction kinetics of acetylene hydrochlorination over Au/NC-473 and Au/AC-473 ($W_{\text{cat}} = 0.05\text{-}0.1$ g, $d_p = 0.4\text{-}0.6$ mm) were studied in the temperature range of 453-483 K with a total flow of 15-20 $\text{cm}^3 \text{ min}^{-1}$ and reactant concentrations of 10-30 vol.% balanced in He. Prior to GC-MS analysis, the catalysts were equilibrated for 45 min. Since vinyl chloride (VCM) was the only product detected in all our tests, the catalytic activity was presented as the yield of VCM, $Y(\text{VCM})$, calculated according to Eq. S1,

$$Y(\text{VCM}) = \frac{n(\text{VCM})^{\text{outlet}}}{n(\text{C}_2\text{H}_2)^{\text{inlet}}} \times 100\% \quad (1)$$

where $n(\text{VCM})^{\text{outlet}}$ and $n(\text{C}_2\text{H}_2)^{\text{inlet}}$ denote the respective molar flows of VCM and C_2H_2 at the reactor outlet and inlet. Each catalytic data point reported is an average of at least two measurements. The carbon mass balance in all catalytic tests closed to >96%.

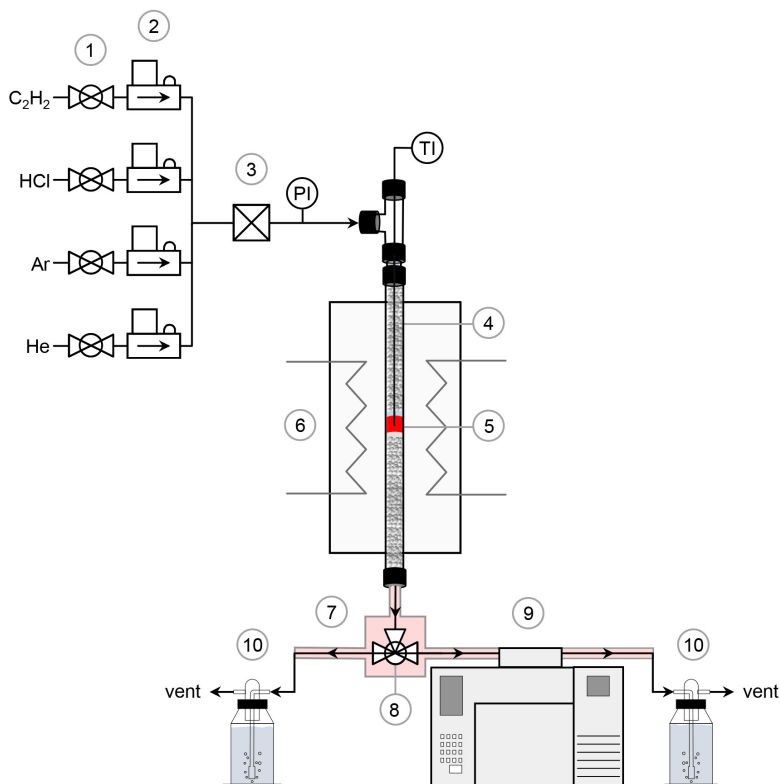


Fig. S1 Scheme of the laboratory set-up used for acetylene hydrochlorination.

Catalyst testing under transient conditions and kinetic analysis

The interactions of C_2H_2 , HCl , and C_2H_3Cl with the bare supports (NC and AC) and selected gold catalysts (Au/NC-473, Au/NC-1073, Au/NC-473-12h, Au/AC-473, Au/AC-673, and Au/AC-473-12h) were studied in the temporal analysis of products (TAP-2) reactor system. This transient pulse technique operates in high vacuum with a time resolution of approximately 100 μs . Each catalyst ($W_{cat} = 13$ mg, $d_p = 0.4$ - 0.6 mm) was packed between two layers of quartz ($d_p = 250$ - 355 μm) within the isothermal zone of an in-house (Leibniz-Institut für Katalyse) developed fixed-bed quartz reactor. Afterwards, the reactor was evacuated stepwise to 10^{-5} Pa. The pulse experiments were carried out at 473 K using $C_2H_2:Ne = 1:1$, $HCl:Ar = 1:1$, and $C_2H_3Cl:Ar = 1:1$ mixtures prepared from C_2H_2 (Air Liquide, 2.6), HCl (Air Liquide, 4.5), VCM (Sigma Aldrich International GmbH, 99.95%), Ne (Linde Gas, 5.0), and Ar (Linde Gas, 5.0) without additional purification. The feed components were quantitatively analysed by an on-line quadrupole mass spectrometer (HAL RC 301 Hiden Analytical). The following atomic mass units (AMUs) were assigned for mass spectrometric identification: 70 (Cl_2), 64 (C_2H_3Cl), 62 (C_2H_3Cl), 36 (HCl), 28 (CO), 27 (C_2H_3Cl , C_2H_2), 26 (C_2H_3Cl , C_2H_2), 22 (Ne), 2 (H_2), 40 (Ar), and 20 (Ar , Ne). The overall pulse size was below 2×10^{15} molecules. Pulses were repeated ten times for each AMU and averaged to improve the signal-to-noise ratio.

To identify the type of adsorption (reversible or irreversible), the obtained transient responses of reactive and inert gases were transformed into a dimensionless form.⁹ The comparison of the relative position of the transformed signals of the inert gas and reactive component allows to distinguish between different types of adsorption. If the transformed signal of reactive component is situated under that of the inert gas, the former adsorbs irreversibly or is consumed. Intersection of the curves indicates reversible adsorption. The obtained responses are summarised in **Fig. S17**.

Kinetic evaluation of the TAP experiments, *i.e.* fitting experimental data to chosen kinetic models, was performed as detailed elsewhere.¹⁰ According to this approach, the TAP micro-reactor is described as a one-dimensional pseudo-homogeneous system. The search for kinetic parameters (reaction constants) was performed in a wide range of possible values (10^{-4} - 10^6) using first a Genetic algorithm¹¹ and subsequently the Nelder-Mead Simplex algorithm.¹² The estimated parameters were validated by applying correlation and sensitivity analyses. The correlation analysis shows if the parameters are

independent from each other, otherwise only their product or ratio can be determined definitively. Since the overall concentration of active sites and the rate constant of adsorption are depending on each other, only their product, denoted as $k_{\text{ads,eff}}$, could be determined. The sensitivity analysis defines an effect of changes of the corresponding parameter on the objective function. When the change of the parameter has no influence on the objective function, the respective reaction step should be refused to avoid over-parameterisation of the model.

Computational methods

Density functional theory (DFT) calculations were performed using the Vienna *Ab initio* simulation package (VASP) code.^{13,14} The functional of choice was Perdew-Becke-Ernzerhof (PBE)¹⁵ with dispersion contributions introduced through the D3 approach.^{16,17} Inner electrons were described by projector augmented-waves (PAW)^{18,19} and the valence monoelectronic states expanded as plane waves with a cutoff kinetic energy of 450 eV. Graphite slabs were modeled using a 6×6 supercell comprising of three layers. Relaxation was allowed in the top two layers and followed by 12 Å of vacuum. The k -points sampling was a Γ -centered 3×3×1 grid ($\sim 0.3 \text{ \AA}^{-1}$). Step edge models were constructed by cleaving the hexagonal graphite unit cell along the (1 1 12) (*zigzag*) and the (1 -1 12) (*armchair*) directions with a slab thickness of $\sim 11 \text{ \AA}$. The bottom third of the slabs was fixed while the top two thirds were allowed to relax. The k -point density was kept similar to the graphite defect models using a 3×1×1 (*zigzag*) and 1×3×1 (*armchair*) grids. A dipole correction was employed along the z direction.²⁰ The molecules were placed in a cubic box of 15 Å sides. In all cases the optimisation thresholds were 10^{-5} and 10^{-4} eV, respectively, for electronic and ionic relaxations. Transition states were located following the climbing image nudged elastic band procedure (CI-NEB).^{21,22} All structures are presented in **Fig. S11** and can be retrieved from the ioChem-BD database²³ following the link:

<https://iochem-bd.iciq.es/browse/review-collection/100/8919/81487888b14938dd7d303e42>

Table S1. Fitting parameters derived from the Au 4f XPS spectra of the Au/NC and Au/AC catalysts.

Catalyst	Au(0) ^a			Au(I) ^a			Au(III) ^a			C 1s reference / eV
	Position / eV	FWHM ^b / eV	Area / %	Position / eV	FWHM / eV	Area / %	Position / eV	FWHM / eV	Area / %	
Au/NC-413	84.2	1.41	100.0	85.0	-	0.0	87.0	-	0.0	285.0 ^c
Au/NC-473	84.2	1.03	46.5	84.8	1.31	53.5	87.0	-	0.0	285.0
Au/NC-573	84.2	0.98	49.2	85.0	1.80	42.9	87.0	2.17	9.9	285.0
Au/NC-673	84.2	0.99	41.6	85.0	1.27	33.2	87.0	2.98	25.2	285.0
Au/NC-973	84.2	1.48	10.3	85.0	1.81	26.3	87.0	1.88	63.4	285.0
Au/NC-1073	84.2	-	0.0	85.0	-	0.0	87.0	2.17	100.0	285.0
Au/AC-413	84.2	1.10	87.6	85.0	0.85	12.4	87.0	-	0.0	284.6
Au/AC-473	84.2	1.10	74.9	85.0	1.43	25.1	87.0	-	0.0	284.6
Au/AC-673	84.2	1.00	100.0	85.0	-	0.0	87.0	-	0.0	284.6
Au/NC-473-12h	84.2	0.96	59.6	84.8	1.01	40.4	87.0	-	0.0	285.0
Au/AC-473-12h	84.2	1.21	71.2	85.0	1.41	28.8	87.0	-	0.0	284.6

^aAssigned based on reference values. ^bFWHM: full width at half maximum. ^cThe higher C 1s binding energy compared to that of the N-free catalysts was due to the creation of the C–N covalent bonds after nitrogen doping.¹⁹

Table S2. Fitting parameters derived from the N 1s XPS spectra of the Au/NC-*T* and reference samples.

Catalyst	N6 ^a			N5 ^a			N3 ^a			N0 ^a			Source
	Position / eV	FWHM / eV	Area / %	Position / eV	FWHM / eV	Area / %	Position / eV	FWHM / eV	Area / %	Position / eV	FWHM / eV	Area / %	
Au/NC-413	398.5	1.48	33.9	400.4	1.84	42.4	401.2	1.66	21.0	403.3	1.65	2.7	This work
Au/NC-473	398.5	1.51	33.3	400.4	1.63	36.4	401.2	1.71	20.2	403.3	3.55	10.2	This work
Au/NC-573	398.5	1.59	32.0	400.4	1.99	37.6	401.2	2.06	22.5	403.3	1.68	7.8	This work
Au/NC-673	398.5	1.51	34.4	400.4	1.63	33.2	401.2	1.44	24.8	403.3	2.86	7.7	This work
Au/NC-973	398.5	1.69	36.1	400.4	1.96	24.7	401.2	1.51	29.2	403.3	2.44	9.9	This work
Au/NC-1073	398.3	1.49	34.1	400.4	1.54	17.9	401.2	1.80	34.6	403.3	2.40	13.2	This work
NC-nanotube	398.3-399.8	n.a.	-	400.1-400.5	n.a.	-	401-402	n.a.	-	404.0-405.6	n.a.	-	ref. 24
NC	n.a.	n.a.	-	399.5	n.a.	-	400.6	n.a.	-	402.9	n.a.	-	ref. 25
N-graphene	398.6	n.a.	-	400.5	n.a.	-	401.3	n.a.	-	402-405	n.a.	-	ref. 26
N,P-carbon	398.6	n.a.	-	400.5	n.a.	-	401.3	n.a.	-	402.0	n.a.	-	ref. 27

^aNitrogen functionalities. N6: pyridinic nitrogen; N5: pyrrolic nitrogen; N3: graphitic nitrogen; N0: oxidised nitrogen. ^bFWHM = full width at half maximum.

Table S3. Fitting parameters derived from the EXAFS data of selected gold catalysts.

Catalyst	Coordination shell	CN^a / -	σ^{2b} / \AA^2	R^c / \AA	R_{eff}^d / \AA	ΔE_0^e / eV
Au/AC-413	Au-Cl	2.5(2)	0.0025(3)	2.269(3)	2.300	8.2(9)
Au/NC-413	Au-Cl	2.0(2)	0.0027(6)	2.272(5)	2.300	9.4(1)
Au/NC-973	Au-N(O)	3.5(8)	0.0100(2)	1.970(2)	1.929	9.0(3)
Au/NC-1073	Au-N(O)	2.7(6)	0.0060(2)	1.980(2)	1.929	10.0(3)

^aCoordination number. ^bDebye-Waller factor. ^cCoordination shell distance. ^dInitial value for the coordination distance in AuCl₃ or Au₂O₃ references used in the fit. ^eEnergy shift. The errors are given in parenthesis. Amplitude reduction factor $S_0^2 = 0.78$.

Table S4. DFT characterisation data of Au and AuCl on the tested defect sites.

Defects site		Au					AuCl					
		E_{form} / eV	Au 4f shift / eV	Bader charge / e ⁻	Distance [Au-*] / Å		E_{form} / eV	Au 4f shift / eV	Bader charge / e ⁻	Distance [Au-*] / Å		
					N	O				Cl	N	O
Graphite		-0.48	0.00	-0.21	2.96*	-	-1.24	3.46	0.38	2.24	2.39*	-
N3		-0.78	0.53	-0.33	2.28	-	-0.61	2.64	0.38	2.22	2.26	-
3×N5		-2.58	1.69	0.55	2.19	-	-2.71	1.21	0.70	2.27	2.09	-
3×NH5		-1.02	1.90	-0.50	3.18	-	-1.38	3.45	0.33	2.24	2.26*	-
N5+2×N6		-1.59	1.72	0.28	2.01	-	-1.98	2.47	0.40	2.22	2.04	-
NH5+2×N6		-0.54	0.15	-0.20	2.93*	-	-1.58	3.14	0.35	2.23	2.10	-
3×N6		-1.48	0.81	0.41	2.34	-	-2.05	2.20	0.46	2.24	2.09	-
4×N6		-3.61	3.67	1.12	1.97	-	-2.39	2.90	1.14	2.79	1.97	-
N0+2×N6		-1.09	0.47	0.30	2.86	2.09	-1.81	2.79	0.42	2.25	2.16	2.23
N0+3×N6		-1.71	2.04	1.05	1.97	1.99	-1.46	1.54	0.43	2.26	2.11	2.40
2×CO		-0.97	0.61	0.20	-	2.11	-1.80	3.36	0.42	2.22	-	2.05
4×CO		-3.25	1.87	0.91	-	2.12	-2.01	1.83	0.60	2.22	-	2.25
Epoxy		-1.32	1.05	0.26	-	2.00	-1.72	2.12	0.42	2.23	-	2.01
2×Epoxy		-1.29	0.70	0.31	-	2.01	-1.77	1.97	0.43	2.23	-	2.02
OH		-2.30	0.90	0.36	-	1.97**	-2.80	2.31	0.40	2.24	-	1.99
2×OH		-0.74	1.28	-0.32	-	3.14	-1.20	3.38	0.37	2.24	-	2.29*
Edge-N5	s2 @N	-0.54	2.03	-0.07	2.23	-	-1.74	2.33	0.30	2.23	2.06	-
Edge-N6	s1 @CN	-0.48	0.96	0.04	2.18*	-	-1.14	3.89	0.36	2.24	2.27*	-
	s3 @2N	-1.51	2.37	0.25	2.30	-	-2.52	3.91	0.40	2.25	2.07	-
Edge-NH6	s1 @C	-1.97	0.65	-0.23	2.16*	-	-2.40	2.67	0.20	2.28	2.06*	-
	s2 @NH	-2.63	2.03	-0.58	3.01	-	-2.01	2.33	0.35	2.23	2.12	-
Edge-OH	s1 @C	-0.51	0.53	-0.10	-	2.20*	-1.30	3.64	0.35	2.24	-	2.25*
	s2 @CH	-0.75	0.88	-0.11	-	2.18*	-1.68	3.80	0.33	2.25	-	2.18*
	s5 @OH	-0.83	1.75	-0.47	-	3.06	-1.33	3.35	0.33	2.21	-	2.14
Edge-CO	s1 @C	-1.10	2.61	0.15	-	2.11*	-1.33	4.06	0.35	2.23	-	2.16*
	s4 @O	-1.22	1.97	0.53	-	2.19	-1.70	2.97	0.66	2.22	-	2.16

Labels correspond to the structures in **Fig. S11**. *C is the closest neighbor, Au-C distance shown; **AuOH molecule adsorbed.

Table S5. Effect of Cl content on the DFT calculated oxidation state descriptors for gold single atom species.

Defect site	Au species	Bader charge / $ e^- $	Au 4 <i>f</i> shift / eV
graphite	Au	0.22	0.00
3×N6	Au	0.41	0.70
	AuCl	0.46	2.20
	AuCl ₂	0.96	2.35
	AuCl ₃	0.83	2.07
	Au	1.05	1.78
N0+3×N6	AuCl	0.43	1.85
	AuCl ₂	0.98	1.83
	AuCl ₃	0.86	2.13
	Au	1.12	3.27
4×N6	AuCl	1.14	2.90
	AuCl ₂	0.99	1.89
	AuCl ₃	0.84	2.14
	Au	1.12	3.27

Table S6. Characterisation data of selected catalysts before and after use in acetylene hydrochlorination.

Catalyst	C ^a / wt. %	H ^a / wt. %	N ^a / wt. %	V _{total} ^b / cm ³ g ⁻¹	V _{micro} ^c / cm ³ g ⁻¹	S _{BET} ^d / m ² g ⁻¹
Au/AC-473	86.7	0.3	0.3	0.60	0.54	1150
Au/AC-473-12h	86.7	0.5	0.3	0.58	0.50	1100
Au/NC-473	68.1	1.3	10.3	0.20	0.14	356
Au/NC-473-12h	72.2	1.4	9.7	0.07	0.02	90
Au/NC-I	71.1	1.5	4.4	0.44	0.26	696
Au/NC-I-12h	73.2	1.1	4.3	0.29	0.07	286
Au/NC-II	76.5	1.0	6.9	0.60	0.32	865
Au/NC-II-12h	79.1	0.9	7.0	0.31	0.12	353
Au/NC-III	83.6	0.4	4.3	0.60	0.37	1005
Au/NC-III-12h	80.6	0.9	3.8	0.57	0.28	801
Au/NC-EtOH	78.5	1.0	10.5	0.30	0.12	331
Au/NC-EtOH-12h	75.0	1.4	9.9	0.27	0.04	198
Au/AC-EtOH	93.3	0.5	0.5	0.81	0.65	1713
Au/AC-EtOH-12h	91.1	0.5	0.4	0.70	0.54	1458

^aElemental analysis. ^bVolume of Ar adsorbed at $p/p_0 = 0.98$. ^c t -plot method. ^dBET method.

Table S7. Reaction schemes of acetylene hydrochlorination on Au(I)Cl single atoms and gold surfaces.

Au(I)Cl single atom			Au surface		
Step		Description	Step		Description
a1-a2	C ₂ H ₂ ads.	*[Cl] + C ₂ H ₂ ↔ C ₂ H ₂ *[Cl]	b1-b2	C ₂ H ₂ ads.	* + C ₂ H ₂ ↔ *C ₂ H ₂
			b2-b3	HCl ads.	* + HCl ↔ *HCl
			b3-b4	HCl diss.	* + *HCl → *H + *Cl
a2-a3	Cl trans.	C ₂ H ₂ *[Cl] → *[C ₂ H ₂ Cl]	b4-b5	H trans.	*H + *C ₂ H ₂ → *C ₂ H ₃ + *
a3-a4	HCl ads.	*[C ₂ H ₂ Cl] + HCl ↔ HCl*[C ₂ H ₂ Cl]	b5-b6	Cl trans.	*C ₂ H ₃ + *Cl → *C ₂ H ₃ Cl + *
a4-a5	H trans.	HCl*[C ₂ H ₂ Cl] → C ₂ H ₃ Cl*[Cl]			
a5-a6	C ₂ H ₃ Cl des.	C ₂ H ₃ Cl*[Cl] ↔ C ₂ H ₃ Cl + *[Cl]	b6-b7	C ₂ H ₃ Cl des.	*C ₂ H ₃ Cl ↔ C ₂ H ₃ Cl + *

*adsorption site; [ligand] coordinated to Au; ads./diss./trans./des/ = adsorption/dissociation/transfer/desorption.

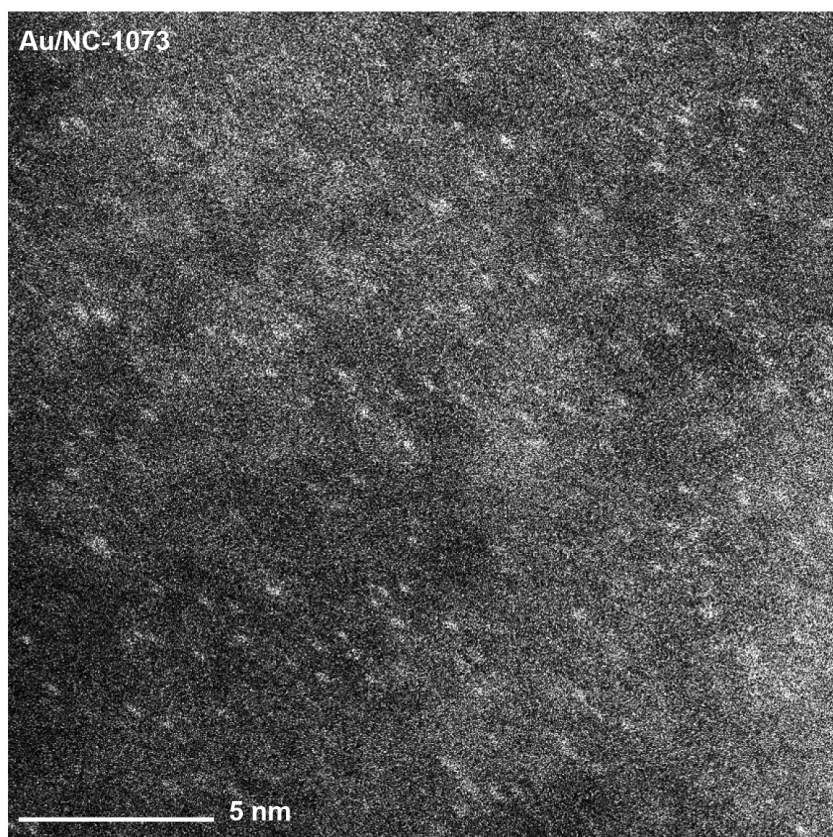
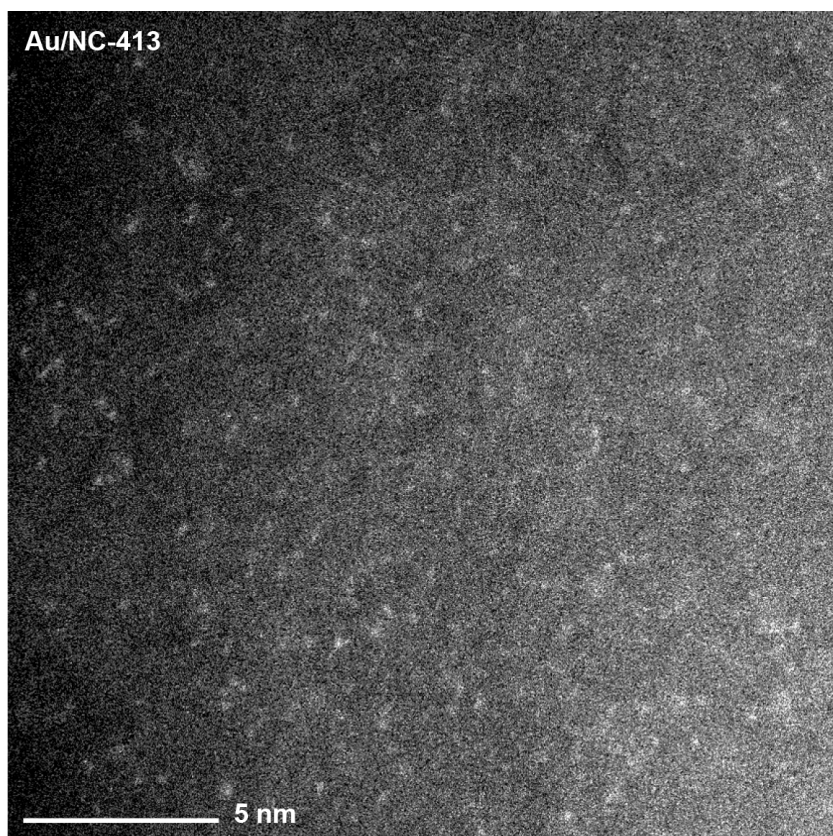


Fig. S2 Additional aberration-corrected STEM images of selected Au/NC-*T* catalysts.

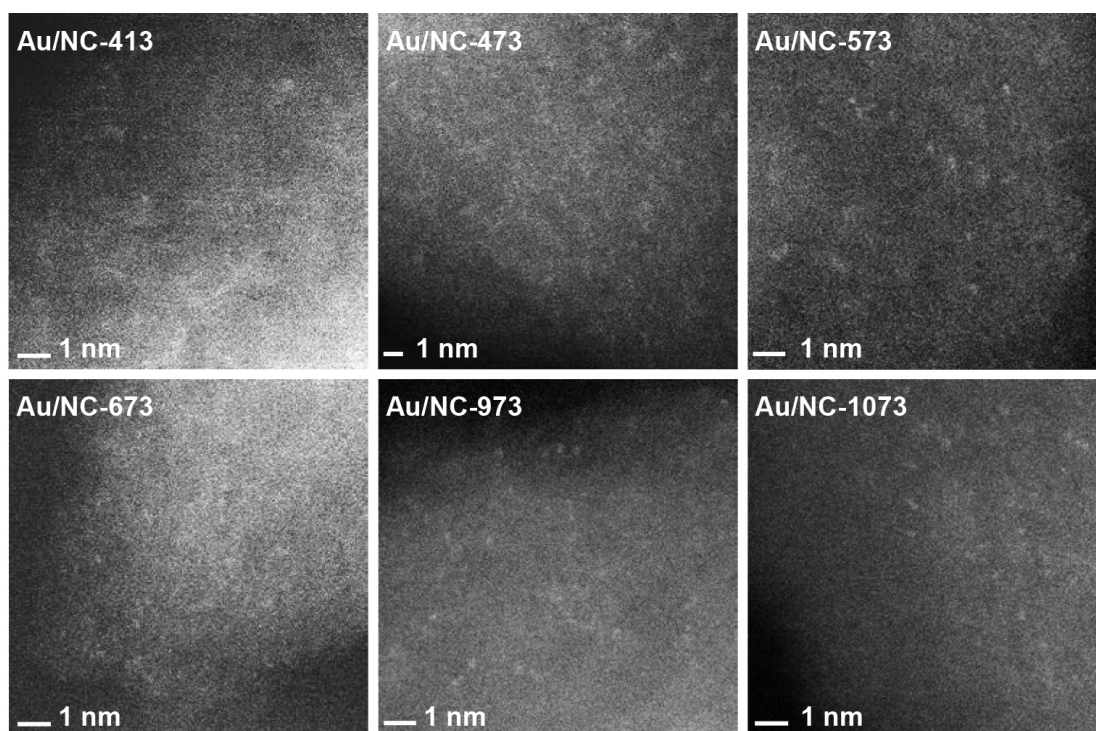


Fig. S3 Additional HAADF-STEM images of selected Au/NC-*T* catalysts.

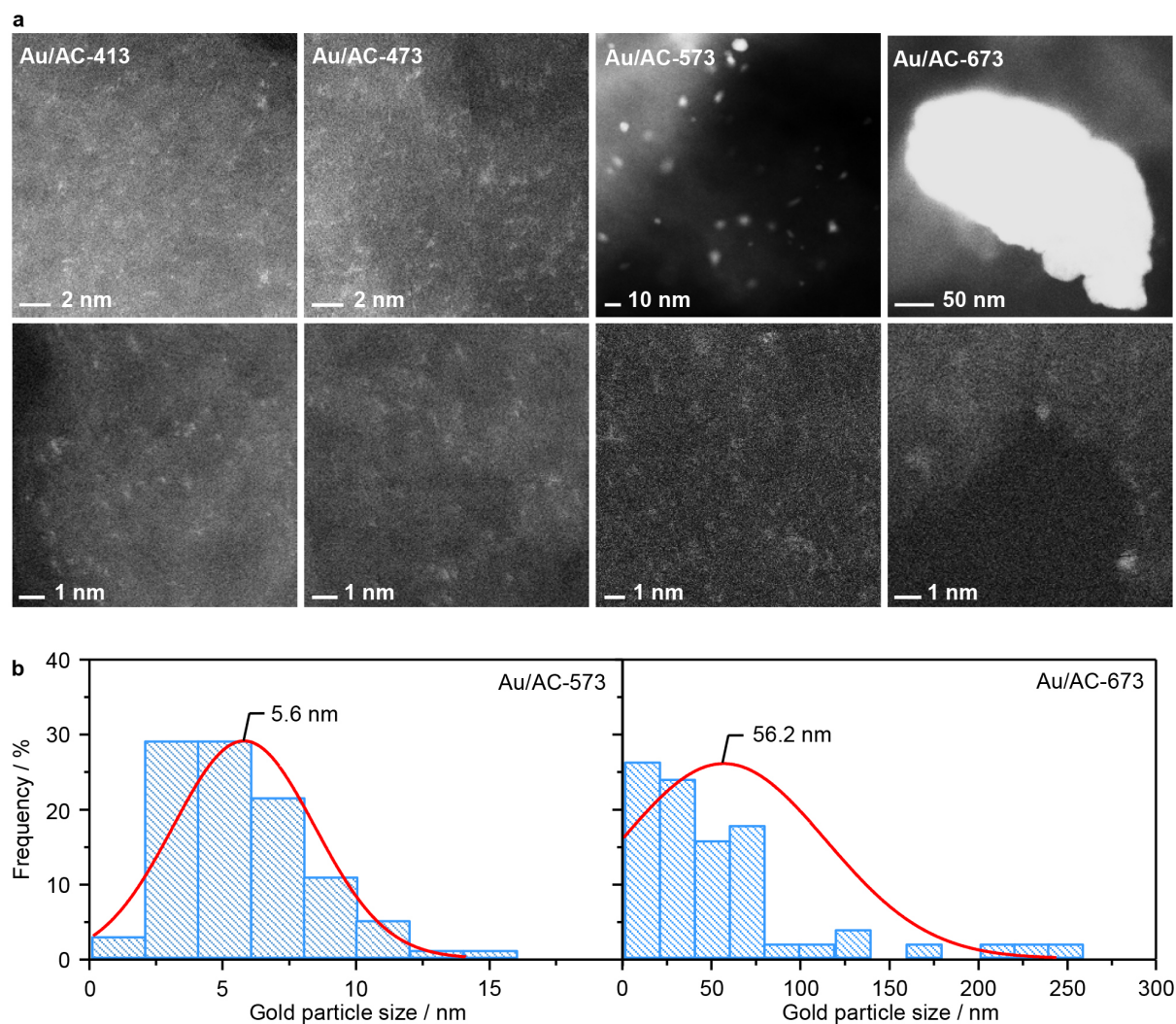


Fig. S4 (a) Additional HAADF-STEM images of selected Au/AC-*T* catalysts. **(b)** Gold particle size distribution in Au/AC-573 and Au/AC-673 (obtained from >100 particles), indicating a relatively narrow distribution at 573 K (mean value of 5.6 nm), while at 673 K rapid particle aggregation occurs.

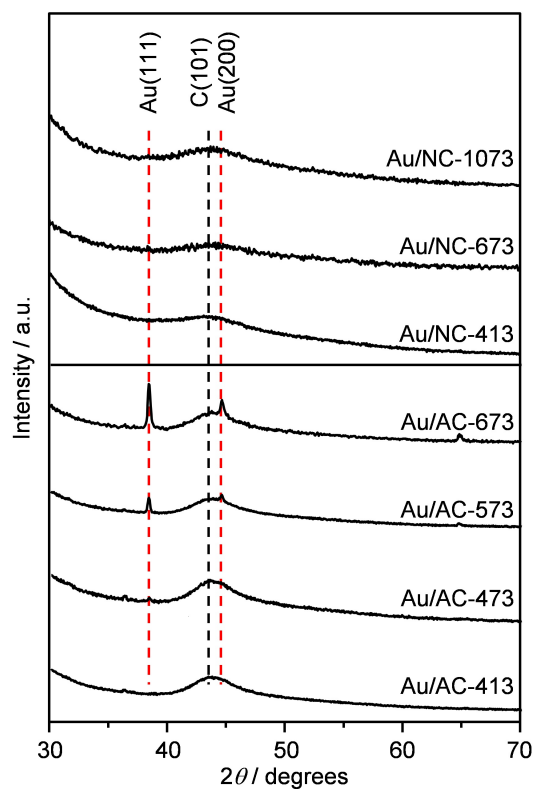


Fig. S5 XRD pattern of the Au/AC catalysts showing a progressive increase of the Au(111) and Au(200) peaks at 38.25° and 44.46° 2θ (vertical dashed red lines) with rising activation temperature, indicating gold particle aggregation. The absence of diffraction lines associated with gold in the Au/NC catalysts indicates the high thermal stability of gold single atoms on the N-doped carbon carrier.

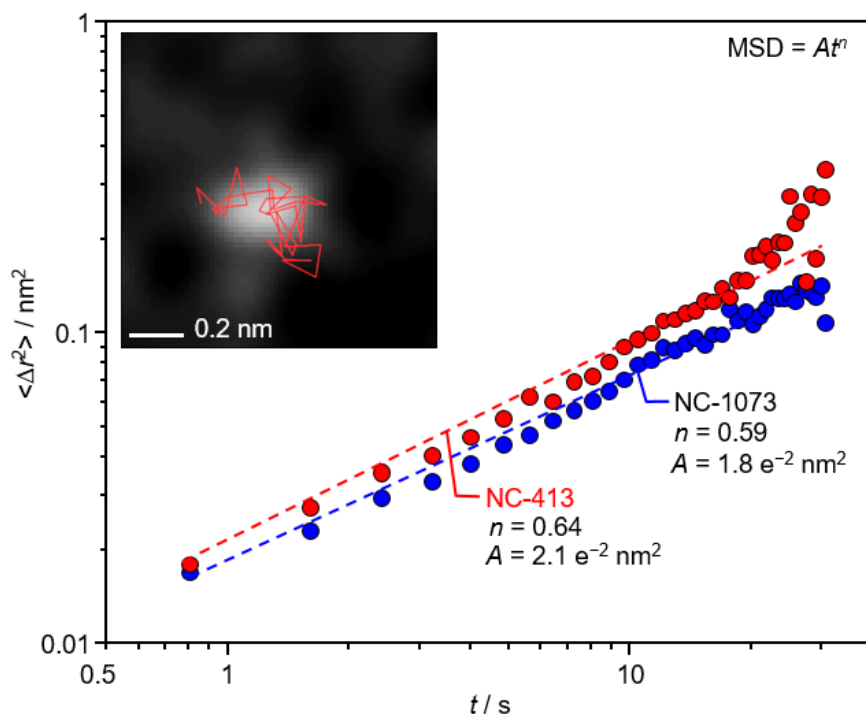


Fig. S6 Ensemble average mean squared displacements (MSD) of gold atoms as a function of imaging time in AC-STEM analysis of Au/NC-413 and Au/NC-1073 samples shown in **Videos S1** and **S2**, respectively. Both samples exhibit significantly lower exponents for the power law dependence of MSD than the value of $n = 1$ expected for random (Brownian) motion. This type of subdiffusion is characteristic of spatial and energetic heterogeneity of coordination sites.⁵ An example trajectory extracted from the AC-STEM video analysis of Au/NC-1073 for a single gold atom, superposed on the first frame of the video, is shown as inset.

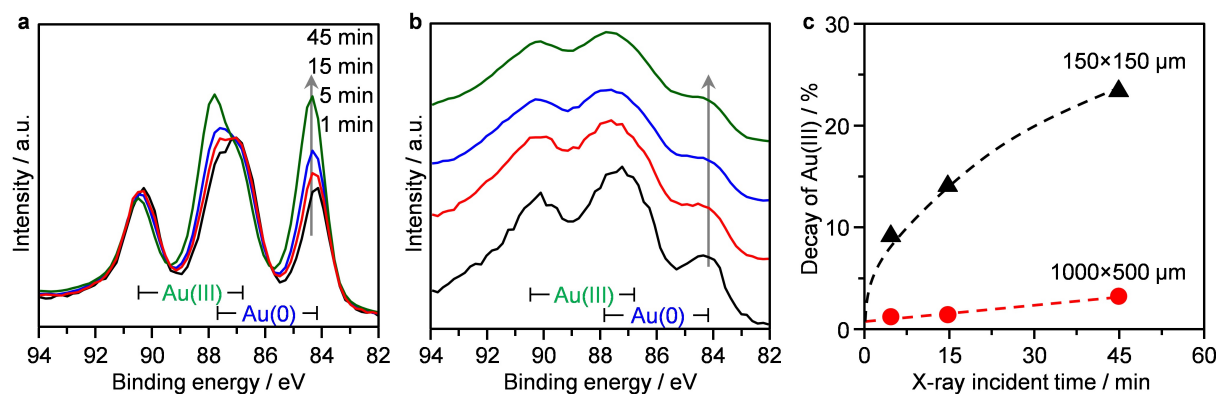


Fig. S7 Evaluation of the photoreduction effect on AuCl_3 . Au 4f X-ray core level spectra obtained at increasing incident time of 1–45 min during spectrum acquisition with varying X-ray dose, as controlled by fixing two different measuring spots of (a) $150 \times 150 \mu\text{m}$ and (b) $1000 \times 500 \mu\text{m}$. (c) Comparison of the Au^{3+} decay with increasing incident time under the two investigated X-ray doses. Since AuCl_3 is light- and moisture-sensitive, cationic Au species are easily reduced to $\text{Au}(0)$ under ambient conditions. Consequently, a large contribution of Au^0 was already detected in the first spectra taken at 1 min, which was used as the reference to evaluate the decay of Au^{3+} due to photoreduction. The decay was calculated as $\text{Au}^{3+} = (\text{Au}^{3+}_{1 \text{ min}} - \text{Au}^{3+}_t) / \text{Au}^{3+}_{1 \text{ min}}$, where Au^{3+}_t and $\text{Au}^{3+}_{1 \text{ min}}$ represent the percentage of Au^{3+} at incident time t and the reference time of 1 min, respectively. The results indicate that the photoreduction effect can be minimised by applying a mild X-ray dose.

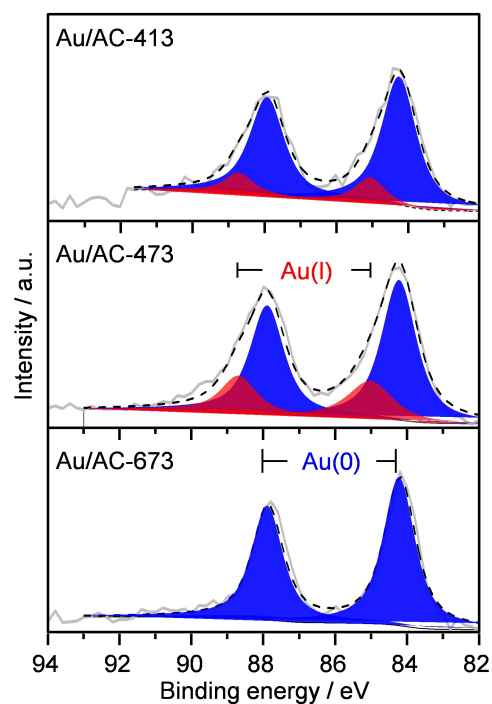


Fig. S8 Au 4f X-ray core level spectra of selected Au/AC-*T* catalysts, indicating an increase in the contribution of Au(0) and a decrease of charged Au species with an increased activation temperature. Dashed black lines show the result of fitting the original data (solid grey lines) and the shaded areas indicate the contributions of distinct Au species.

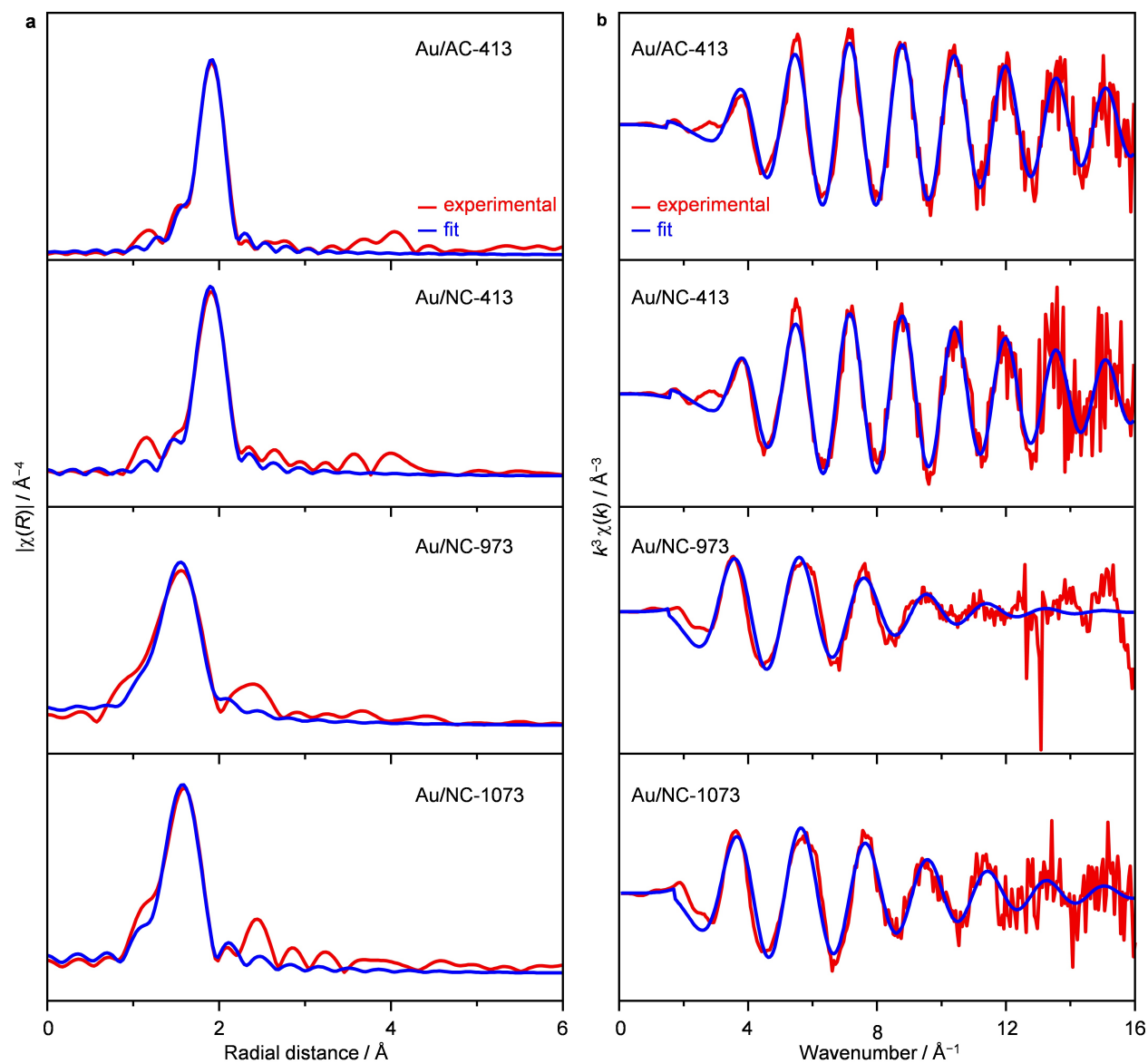


Fig. S9 Experimental and fitted EXAFS spectra at the Au L_3 -edge for selected gold catalysts.

(a) R -space, and (b) k -space.

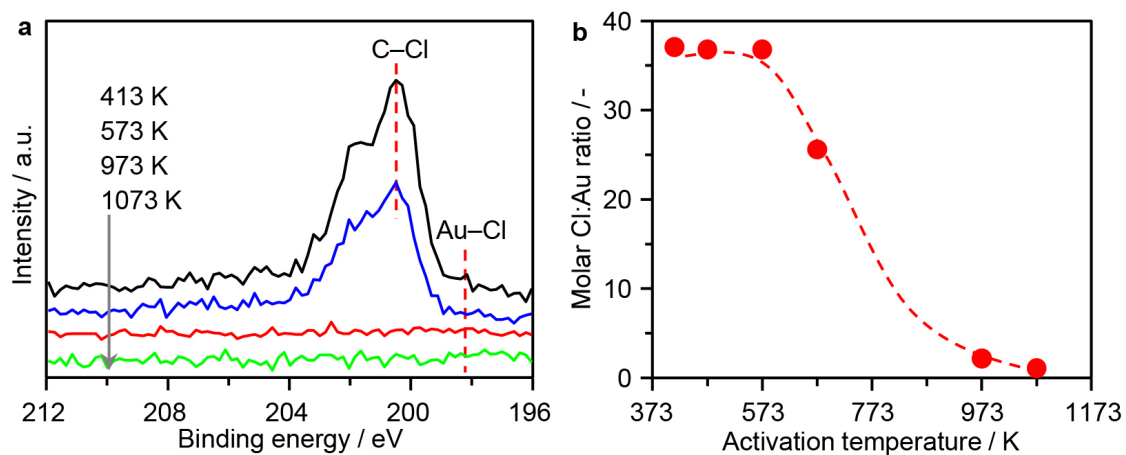


Fig. S10 (a) Cl 2p X-ray core level spectra and (b) molar Cl:Au ratio at the surface of the Au/NC-*T* catalyst after activation at different temperatures. The red dashed lines in **a** indicate the positions of distinct chloride species.

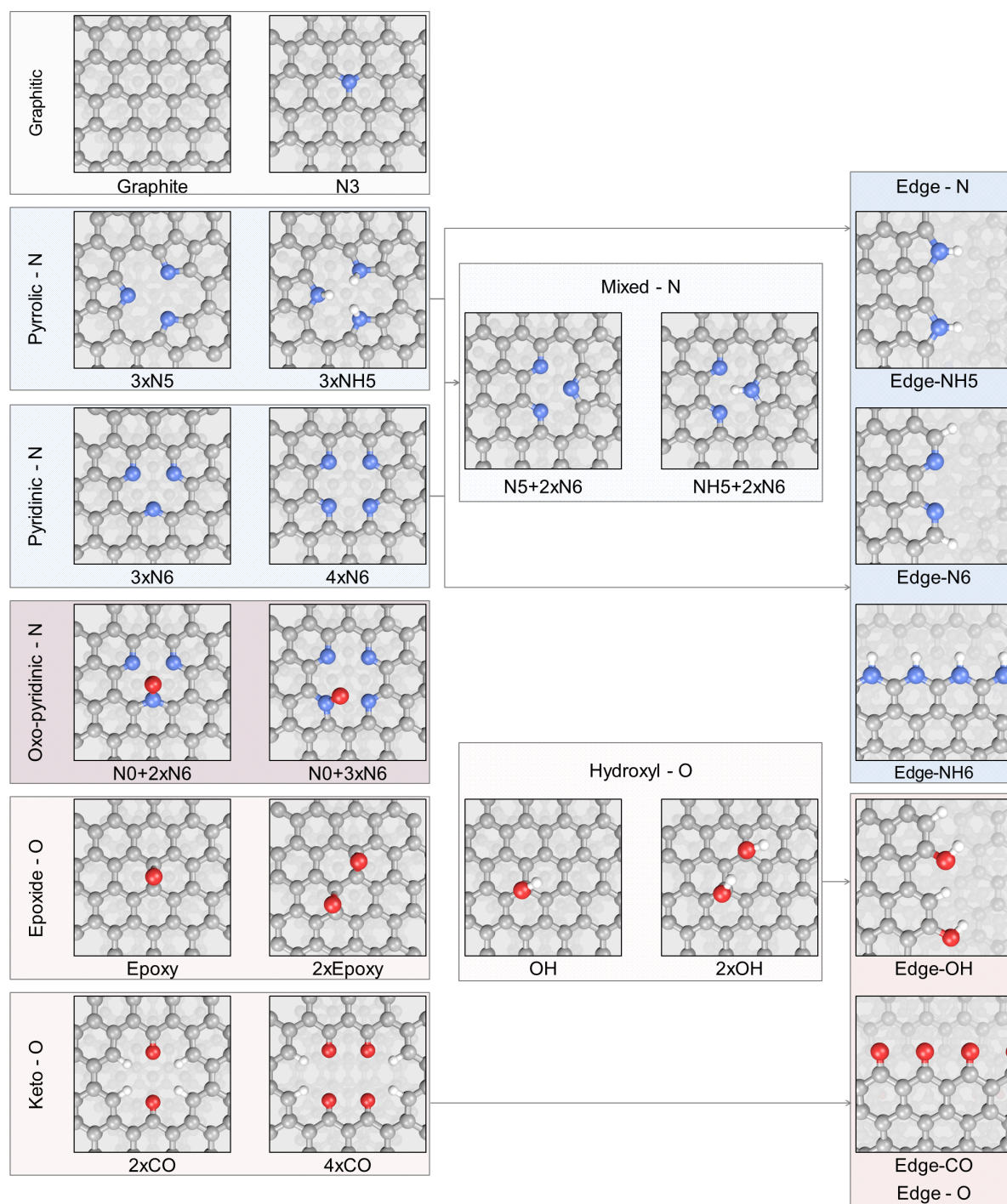


Fig. S11 Schematic representation of the investigated gold nesting points on N-doped carbon.

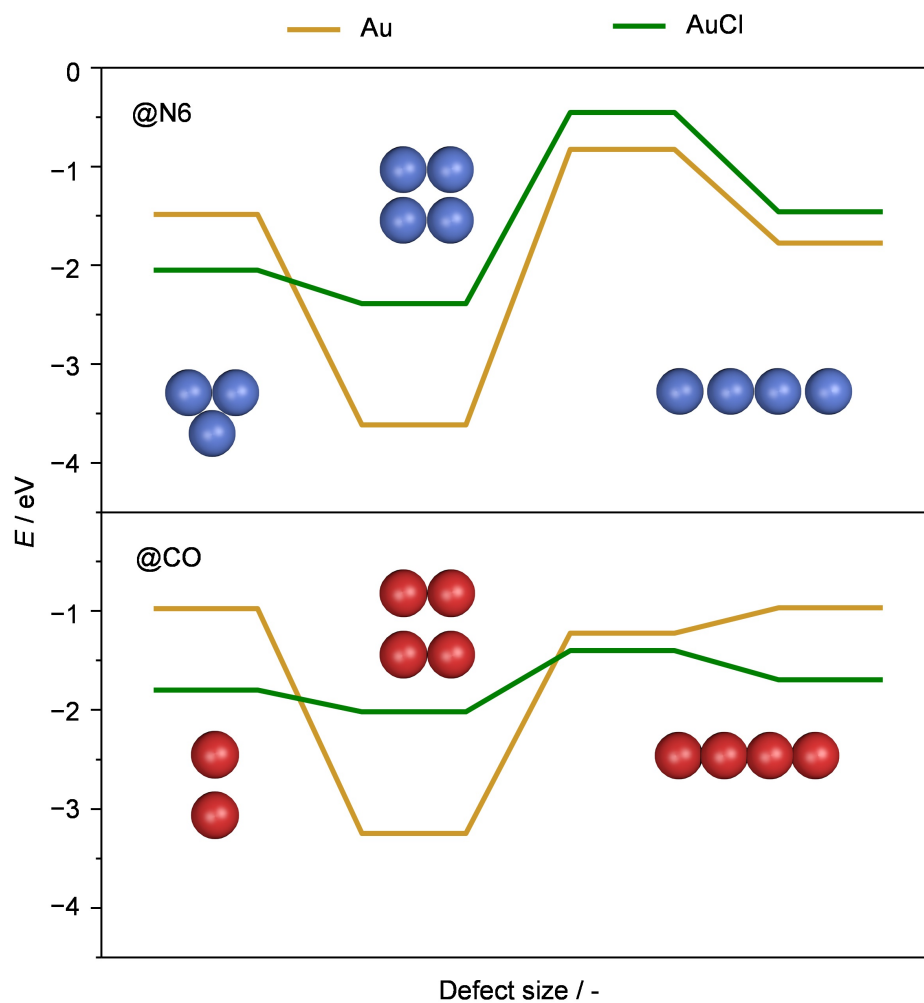


Fig. S12 Effect of the cavity size on the formation energies of Au (yellow) and AuCl (green) on pyridinic (top) and keto defects (bottom) ranging from the smallest possible to step edges (infinitely large defects) from left to right.

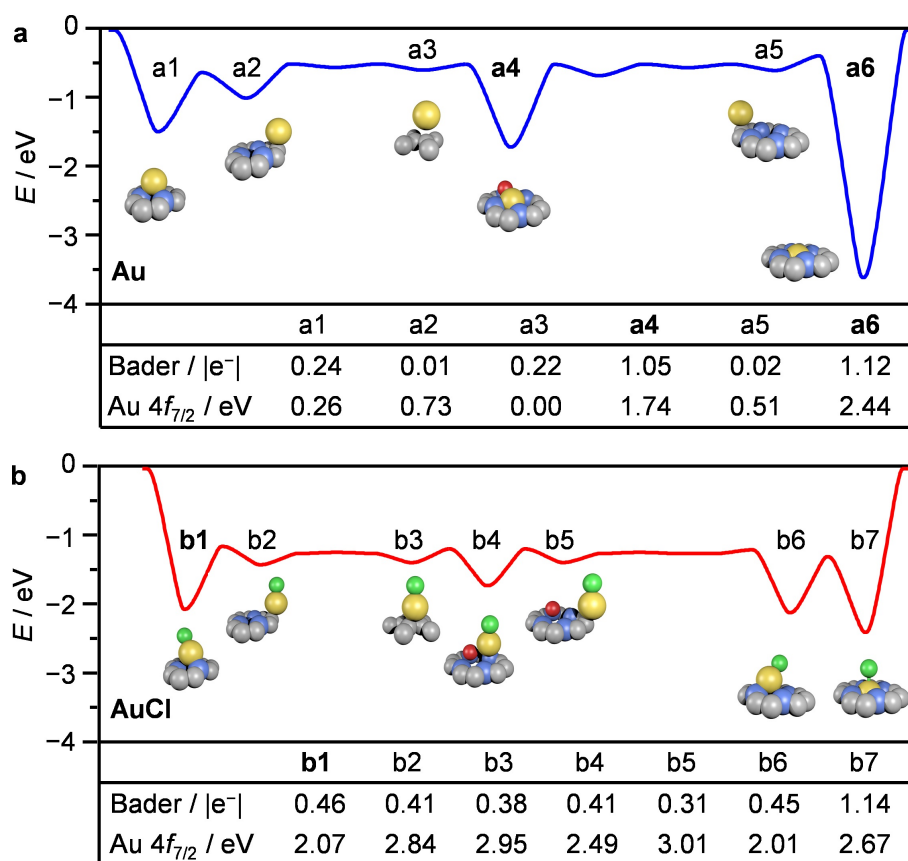


Fig. S13 Energy profiles for the surface diffusion of **(a)** Au and **(b)** AuCl between 3×N6, graphite, 3×N6+N0 and 4×N6, with the Bader charges and Au 4f XPS shifts (relative to a gold atom on the graphite basal plane) presented in the bottom panel. The most representative gold species are highlighted in bold.

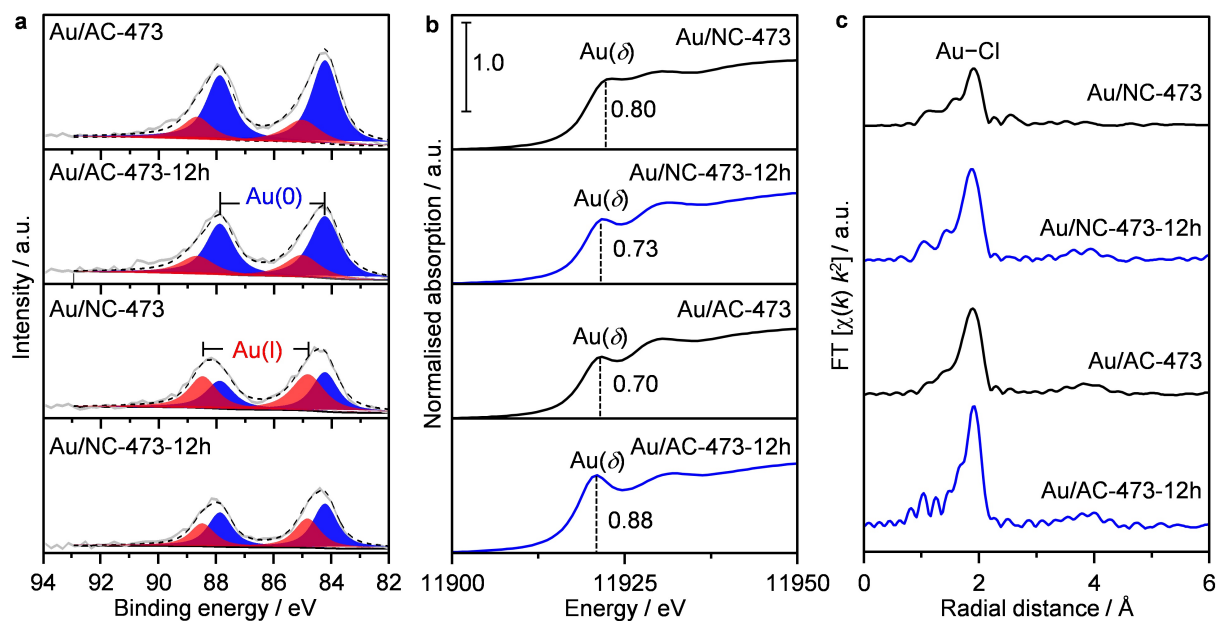


Fig. S14 Analysis of the gold speciation in the as-prepared Au/AC-473 and Au/NC-473 catalysts and after use in acetylene hydrochlorination for 12 h based on (a) Au 4f core level XPS, (b) Au L_3 edge-normalised XANES, and (c) Fourier transform EXAFS spectra. Dashed black lines in **a** show the result of fitting the original data (solid grey lines) and the shaded areas depict the contributions of distinct gold species. Vertical dashed lines in **b** indicate the white line intensity of the distinct cationic gold species $I < \delta < III$.

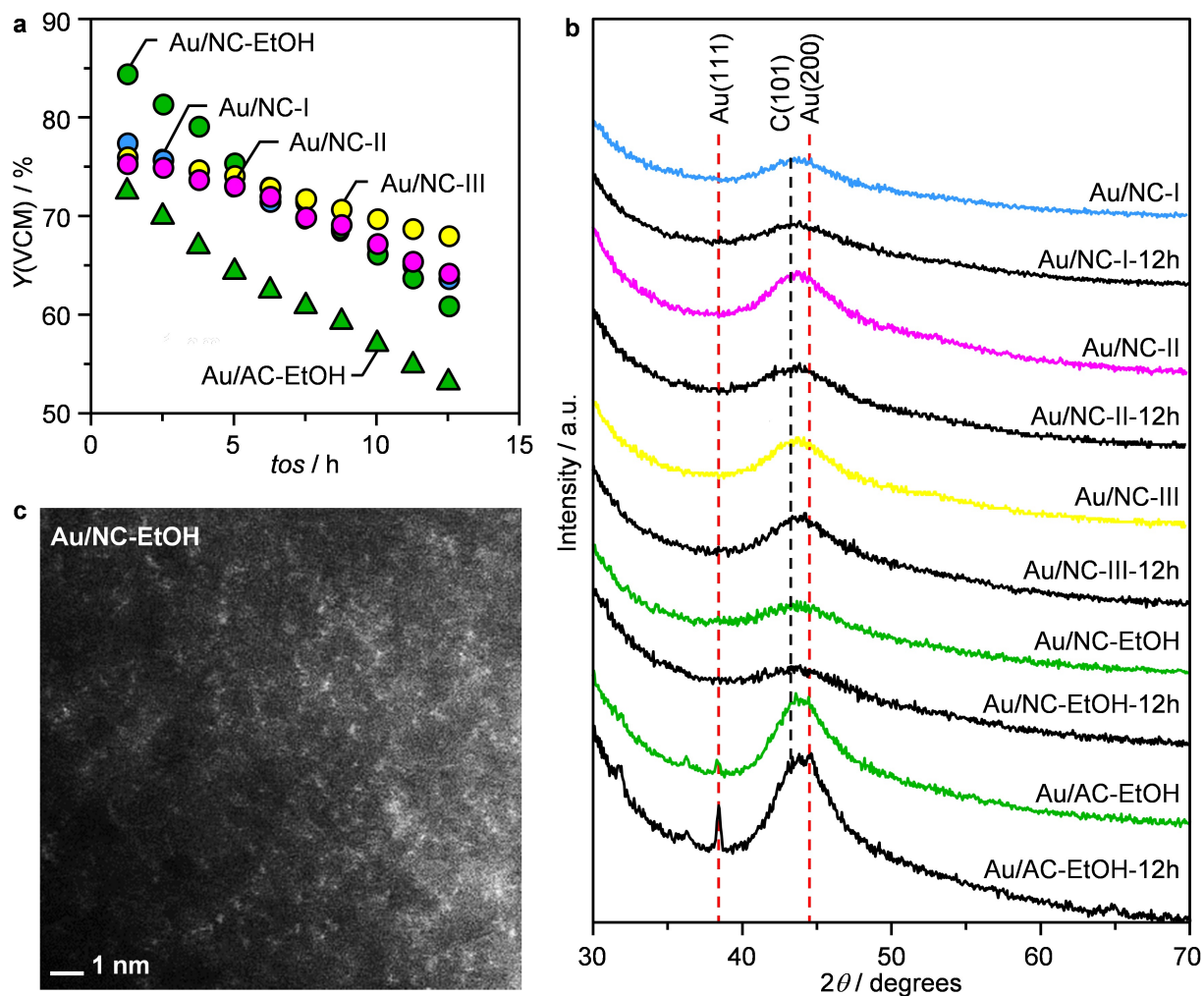


Fig. S15 (a) Time-on-stream (tos) in acetylene hydrochlorination over selected N-doped carbon supported Au catalysts. (b) XRD patterns of the as-prepared samples and after 12 h tos , showing the development of the Au(111) and Au(200) diffraction peaks (vertical dashed red lines) for Au/AC-EtOH. (c) HAADF-STEM micrograph of the as-prepared Au/NC-EtOH sample, revealing the atomic dispersion of gold. Reaction conditions: $T = 473 \text{ K}$, $W_{\text{cat}} = 0.25 \text{ g}$, $\text{HCl}:\text{C}_2\text{H}_2:\text{Ar} = 44:40:16$, $F_T = 15 \text{ cm}^3 \text{ min}^{-1}$, and $P = 1 \text{ bar}$.

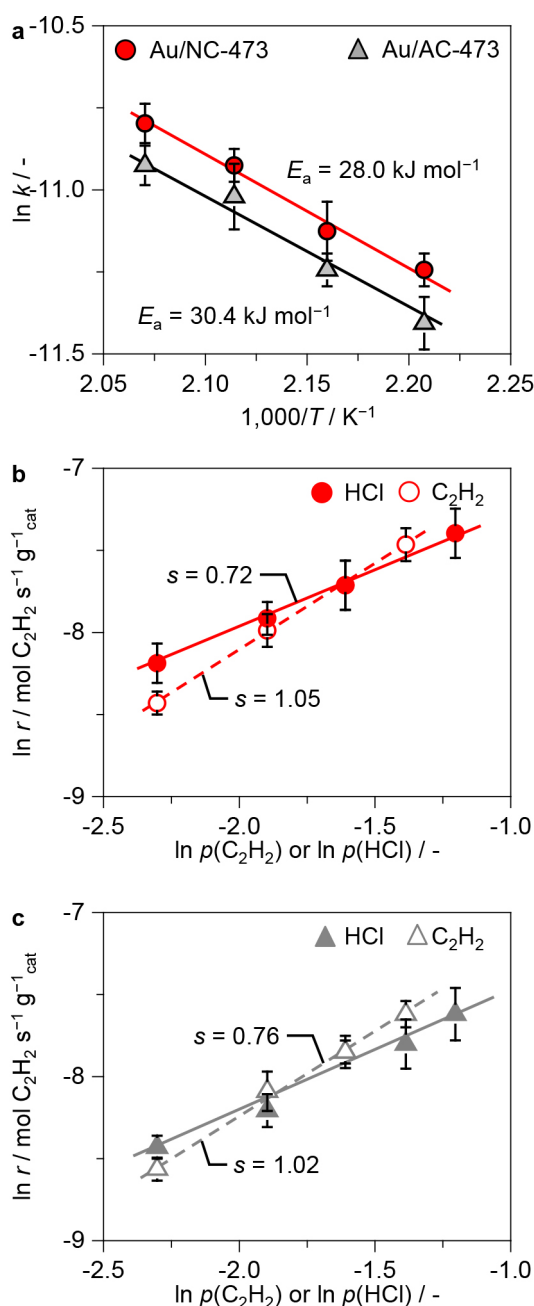


Fig. S16 Reaction kinetics of acetylene hydrochlorination on Au/NC-473 and Au/AC-473.

(a) Arrhenius plots for the reaction rate constants, k , used to derive the apparent activation energy, E_a .

(b, c) Reaction rate, r , as a function of the partial pressure of C₂H₂ or HCl. The partial reaction order of both reactants is indicated by the slope (s) of the fitting lines. Reaction conditions: $T = 473 \text{ K}$, $F_T = 20 \text{ cm}^3 \text{ min}^{-1}$, $W_{\text{cat}} = 0.08 \text{ g}$, and $P = 1 \text{ bar}$. All kinetic studies were performed at a yield level of vinyl chloride $< 20\%$, where external and internal mass transfer limitations could be excluded. In order to circumvent the influence of catalyst deactivation, each point was obtained in a single experiment.

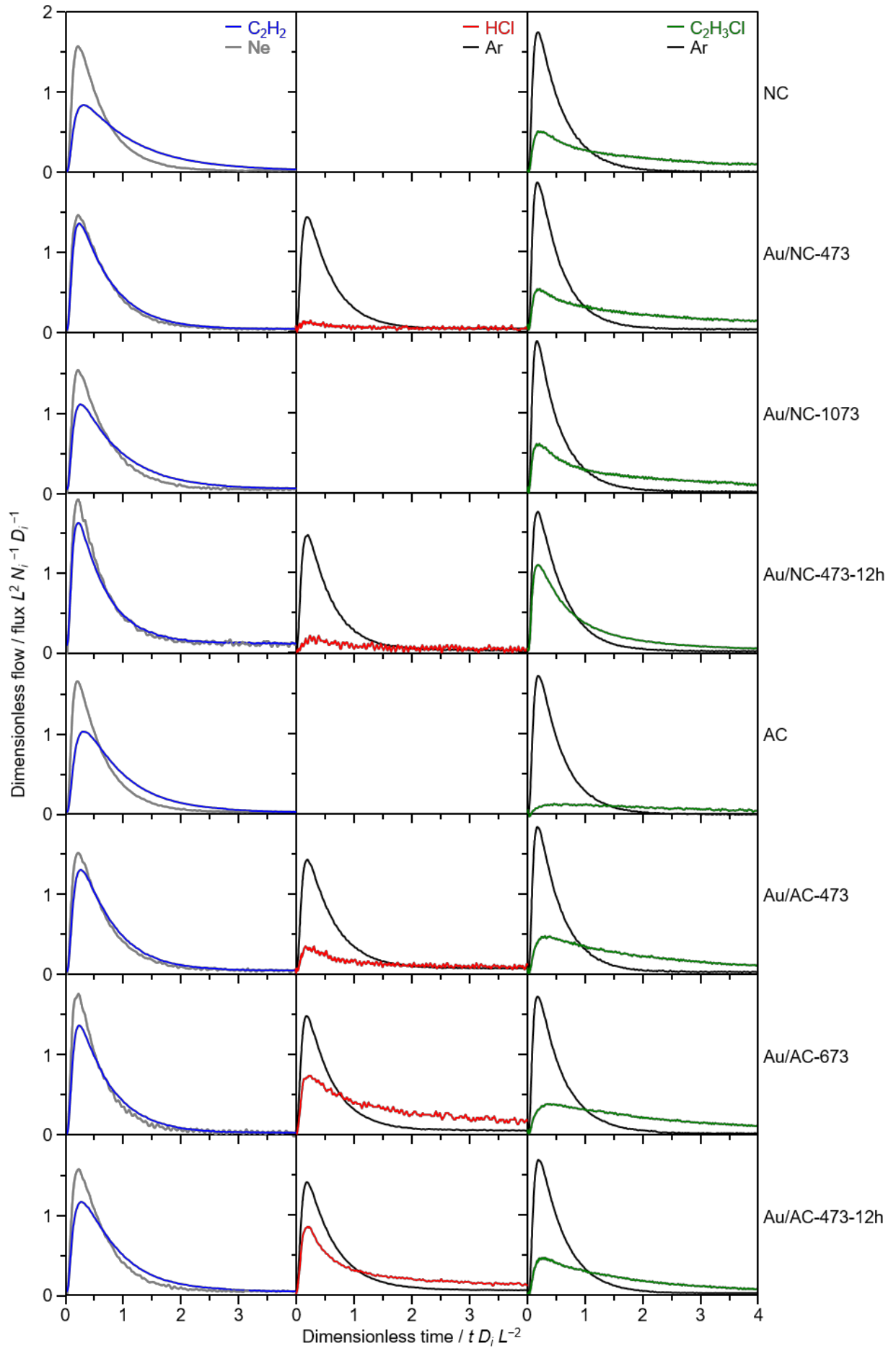


Fig. S17 Transient responses of reactive (C_2H_2 , HCl , and $\text{C}_2\text{H}_3\text{Cl}$), and inert gases (Ne , or Ar) upon single pulsing of $\text{C}_2\text{H}_2:\text{Ne} = 1:1$, $\text{HCl}:\text{Ar} = 1:1$, and $\text{C}_2\text{H}_3\text{Cl}:\text{Ar} = 1:1$, respectively, at 473 K over selected gold catalysts. The data was transformed into a dimensionless form to exclude diffusivity effects of compounds with different molecular weights. Irrespective of the presence or speciation of gold, the majority of dimensionless responses of C_2H_2 , HCl or $\text{C}_2\text{H}_3\text{Cl}$ crossed the corresponding responses of the inert gases, indicating reversible adsorption on all the samples. Only on bare supports (AC and NC) and Au/NC-1073 , HCl adsorbed irreversibly or was consumed, as no response signal was detected at the reactor outlet (empty boxes).


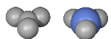
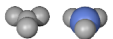
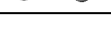

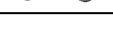




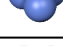

Defect	NC			Au/NC - 473			Au/NC - 1073		
	Au/AuCl population	E_{HCl} / eV	$E_{\text{C}_2\text{H}_2}$ / eV	Au/AuCl population	E_{HCl} / eV	$E_{\text{C}_2\text{H}_2}$ / eV	Au/AuCl population	E_{HCl} / eV	$E_{\text{C}_2\text{H}_2}$ / eV
Graphite		-0.19	-0.13		-0.19	-0.13		-0.19	-0.13
N3		-0.16	-0.16		-0.16	-0.16		-0.16	-0.16
3xN5		-1.62	-0.34		-0.38	-1.19		-1.62	-0.34
N5+2N6		-0.98	-0.11		-0.82	-0.59		-0.98	-0.11
3xN6		-1.14	-0.15		-0.46	-0.26		-1.14	-0.15
N0+2xN6		-0.47	-0.03		-0.41	-0.16		-0.47	-0.03
N0+3xN6		-0.46	-0.05		-0.29	-0.21		-0.29	-0.21
4xN6		-0.58	-0.13		-0.16	-0.19		-0.16	-0.19

Fig. S18 Heatmap for the adsorption energies of HCl and C₂H₂ on different unoccupied and occupied defects. Grey corresponds to low and red/blue to high adsorption of HCl/C₂H₂. On NC, gold is not present and the defects remain unpopulated. The adsorption of HCl on empty defects is strong due to the N–H interaction, and in some cases leads to dissociative adsorption which is likely irreversible. On Au/NC-473 the defects are occupied mostly by AuCl. These ensembles adsorb HCl weaker in comparison to the naked sites. High-temperature treatment of the catalysts leads to the removal of Cl and the migration of gold atoms to the 4×N6 cavities in Au/NC-1073. This migration leaves the ‘3×N*’ cavities unpopulated and free to interact with HCl. Hence, this sample shows high/irreversible adsorption of HCl. The adsorption energies of C₂H₂ are mainly in the physisorption regime, except for a few cases (*e.g.*, C₂H₂ activation). However, for Au coordinated with two or three Cl atoms (AuCl₂ or AuCl₃), lower adsorption of C₂H₂ can be expected.²⁸

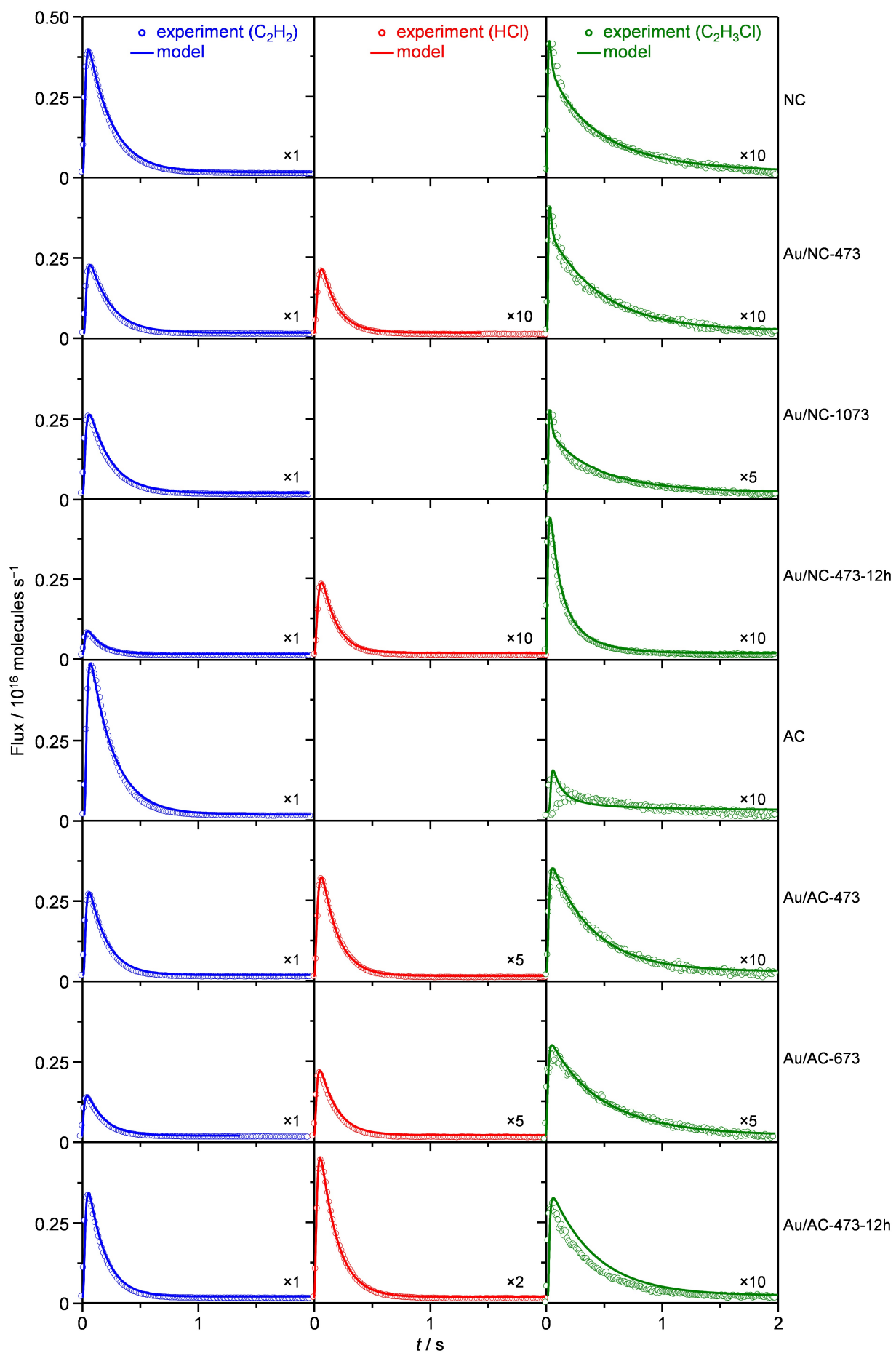


Fig. S19 A comparison between experimental and simulated responses of C₂H₂, HCl, and C₂H₃Cl (Fig. S17) obtained by using the following reversible adsorption model:



A = C₂H₂, HCl, or C₂H₃Cl, *: adsorption site. The adsorption and desorption constants, $k_{\text{ads,eff}}$ and k_{des} , are given in **Table 2**. In the case of NC, AC, and Au/NC-1073 no fitting procedure could be applied due to the irreversible adsorption or consumption of HCl (empty boxes).

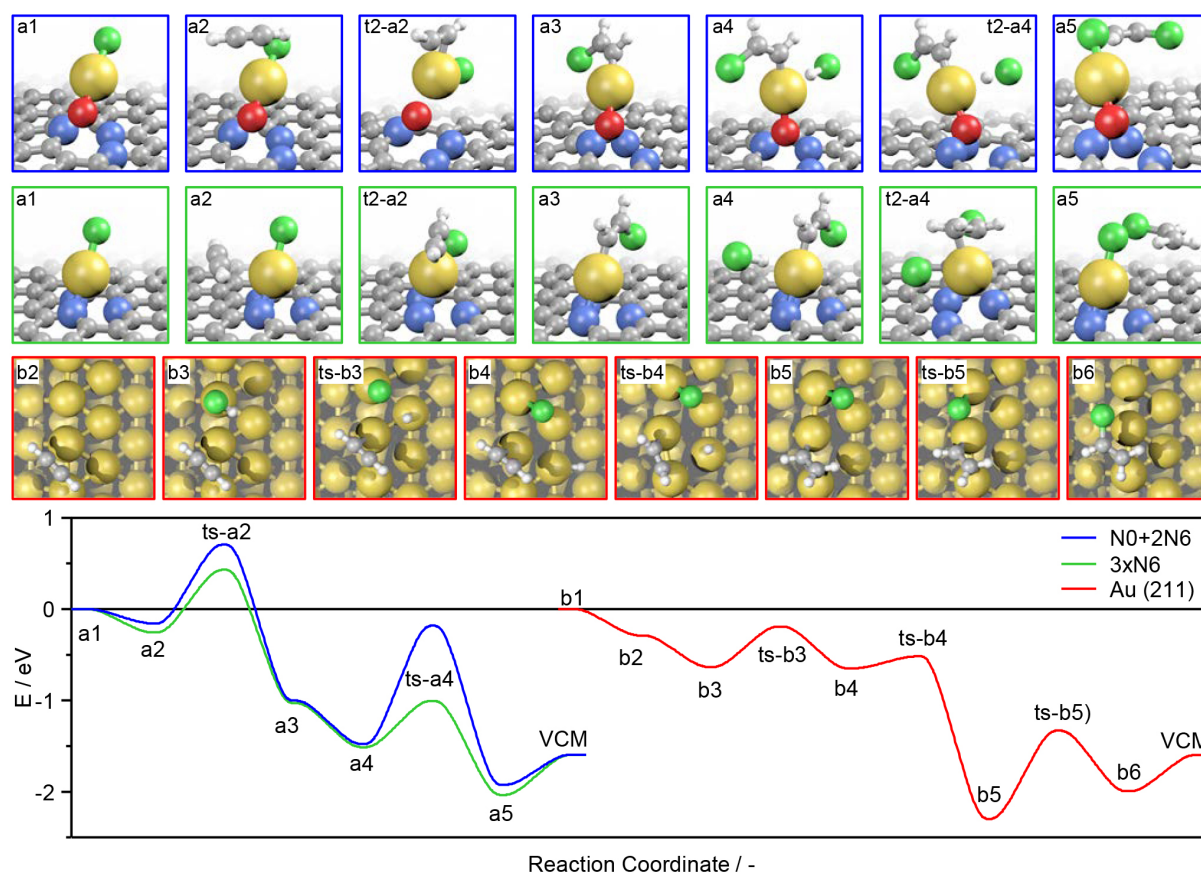


Fig. S20 The whole reaction cycle of acetylene hydrochlorination over selected catalyst models for (i) Au(I)Cl single atoms on the 3-fold pyridinic-N ($3\times N6$, green pathway) and the oxidised pyridinic and two pyrrolic-N-site ($N0+2\times N5$, blue pathway), and (ii) the Au(211) surface (red pathway), accompanied by the geometries for intermediates and transition states (ts) for all sites. As the reaction mechanism over gold single atoms and gold nanoparticles are very similar, respectively, the representative adsorption models and transient states given here are in line with those displayed in **Fig. 5**.

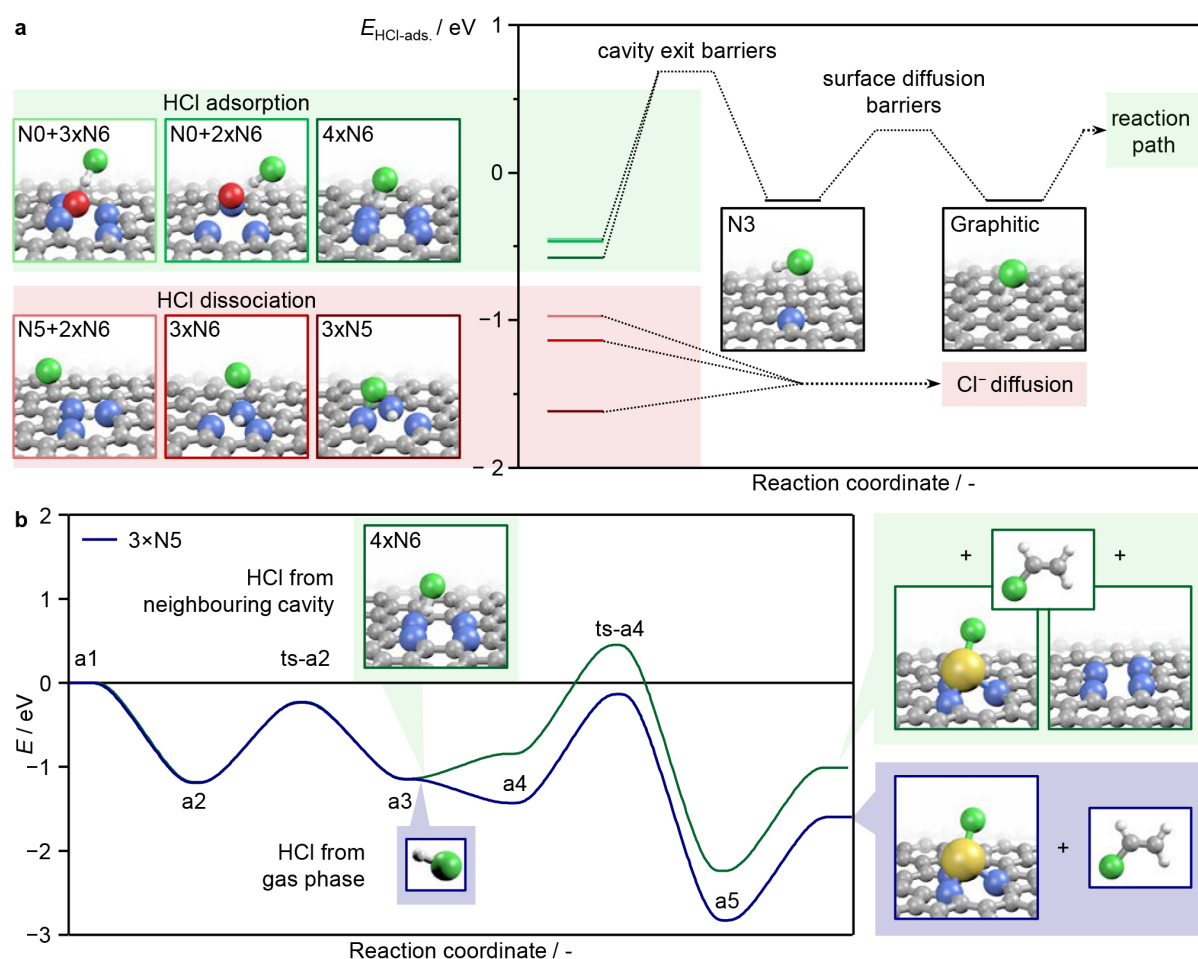


Fig. S21 (a) Adsorption energies of HCl on different CN cavities showing non-dissociative or dissociative mechanisms. If the Cl-H bond is broken, a new N-H bond is formed and the Cl ion remains either (i) adsorbed on the cavity or (ii) mobile on the surface if sufficient thermal energy is provided. Molecular HCl can exit the cavity as well, “hopping” onto the graphitic basal plane in an endothermic process. This mobility of HCl can yield an active gold site which promotes the reaction mechanism as described in **Fig. 5**. **(b)** Impact of the origin of HCl on the reaction profile over AuCl@pyrrolic defect (3xN5, reaction profile identical to **Fig. 5**). The mechanism proceeds as described in the main manuscript, with the difference that reacting a HCl molecule from a neighbouring cavity shifts the second part of the reaction profile up (green line) for the value of the HCl adsorption energy on the CN cavity (here shown for 4xN6).

Supplementary Video Captions

Video S1 AC-STEM image series of Au/NC-413 with exposure time to the X-ray beam.

Video S2 AC-STEM image series of Au/NC-1073 with exposure time to the X-ray beam.

References

- 1 R. Lin, S. K. Kaiser, R. Hauert and J. Pérez-Ramírez, *ACS Catal.*, 2018, **8**, 1114.
- 2 M. Conte, C. J. Davies, D. J. Morgan, T. E. Davies, D. J. Elias, A. F. Carley, P. Johnston and G. J. Hutchings, *J. Catal.*, 2013, **297**, 128.
- 3 X. Liu, M. Conte, D. Elias, L. Lu, D. J. Morgan, S. J. Freakley, P. Johnston, C. J. Kiely and G. J. Hutchings, *Catal. Sci. Technol.*, 2016, **6**, 5144.
- 4 Z. Chen, S. Mitchell, E. Vorobyeva, R. K. Leary, R. Hauert, T. Furnival, Q. M. Ramasse, J. M. Thomas, P. A. Midgley, D. Dontsova, M. Antonietti, S. Pogodin, N. López and J. Pérez-Ramírez, *Adv. Funct. Mat.*, 2017, **27**, 1605785.
- 5 T. Furnival, R. K. Leary, E. C. Tyo, S. Vajda, Q. M. Ramasse, J. M. Thomas, P. D. Bristowe and P. A. Midgley, *Chem. Phys. Lett.*, 2017, **683**, 370.
- 6 P. M. Abdala, O. V. Safonova, G. Wiker, W. van Beek, H. Emerich, J. A. van Bokhoven, J. Sá, J. Szlachetko and M. Nachttegaal, *Chimia*, 2012, **66**, 699.
- 7 O. Müller, M. Nachttegaal, J. Just, D. Lützenkirchen-Hecht and R. Frahm, *J. Synchrotron Rad.*, 2016, **23**, 260.
- 8 M. Newville, *J. Synchrotron Rad.*, 2001, **8**, 322.
- 9 J. T. Gleaves, G. S. Yablonskii, P. Phanawadee and Y. Schuurman, *Appl. Catal., A*, 1997, **160**, 55.
- 10 M. Soick, D. Wolf and M. Baerns, *Chem. Eng. Sci.*, 2000, **55**, 2875.
- 11 M. Baerns, O. V. Buyevskaya, L. Mleczko and D. Wolf, *Stud. Surf. Sci. Catal.*, 1997, **107**, 421.
- 12 W. H. Press, B. P. Flannery, S. A. Teukolsky and W. T. Vetterling, *Numerical Recipes in FORTRAN*, Cambridge University Press, Cambridge, 1992.
- 13 G. Kresse and J. Furthmüller, *Comput. Mater. Sci.*, 1996, **6**, 15.
- 14 G. Kresse and J. Furthmüller, *Phys. Rev. B*, 1996, **54**, 11169.
- 15 J. P. Perdew, K. Burke, and M. Ernzerhof, *Phys. Rev. Lett.*, 1996, **77**, 3865.
- 16 S. Grimme, *J. Comput. Chem.*, 2006, **27**, 1787.
- 17 S. Grimme, J. Antony, S. Ehrlich and H. Krieg, *J. Chem. Phys.*, 2010, **132**, 154104.
- 18 P. E. Blöchl, *Phys. Rev. B*, 1994, **50**, 17953.
- 19 G. Kresse and D. Joubert, *Phys. Rev. B*, 1999, **59**, 1758.
- 20 G. Makov and M. C. Payne, *Phys. Rev. B*, 1995, **51**, 4014.
- 21 G. Henkelman, B. P. Uberuaga and H. Jonsson, *J. Chem. Phys.*, 2000, **113**, 9901.
- 22 G. Henkelman and H. Jonsson, *J. Chem. Phys.*, 2000, **113**, 9978.

- 23 M. Álvarez-Moreno, C. de Graaf, N. López, F. Maseras, J. M. Poblet, and C. Bo, *J. Chem. Inf. Model.*, 2015, **55**, 95.
- 24 K. Zhou, B. Li, Q. Zhang, J. Q. Huang, G. L. Tian, J. C. Jia, M. Q. Zhao, G. H. Luo, D. S. Su and F. Wei, *ChemSusChem*, 2014, **7**, 723.
- 25 J. W. F. To, Z. Chen, H. Yao, J. He, K. Kim, H.-H. Chou, L. Pan, J. Wilcox, Y. Cui and Z. Bao, *ACS Cent. Sci.*, 2015, **1**, 68.
- 26 W. Ding, Z. D. Wei, S. G. Chen, X. Q. Qi, T. Yang, J. S. Hu, D. Wang, L. J. Wan, S. F. Alvi and L. Li, *Angew. Chem. Int. Ed.*, 2013, **52**, 11755.
- 27 J. Zhang, Z. Zhao, Z. Xia and L. Dai, *Nat. Nanotechnol.*, 2015, **10**, 444.
- 28 M. García-Mota, N. Cabello, F. Maseras, A. M. Echavarren, J. Pérez-Ramírez and N. Lopez, *ChemPhysChem*, 2008, **9**, 1624.